Nanoscale

PAPER

View Article Online
View Journal | View Issue

Cite this: *Nanoscale*, 2025, **17**, 1371

Portfolio of colloidally stable gold–gold sulfide nanoparticles and their use in broad-band photoacoustic imaging†

Mine Demir, ‡[a] M. Natali Çizmeciyan, *‡[b,c,d] Dilara Sipahioğlu,[a] Alireza Khoshzaban,[b] M. Burçin Ünlü *[d] and Havva Yağcı Acar *[a]

There is an increasing interest in non-invasive photoacoustic imaging and hence demand for non-toxic, stable, optical solid absorbers, particularly in the visible and near-infrared regions enabling deep tissue penetration. The most popular gold nanorods (GNR) suffer from cumbersome synthesis with poor reproducibility and stability under moderate laser exposure. Recently, a new class of nanoparticle, gold–gold sulfide (GGS), was recognized to have strong NIR absorption but lack colloidal stability. Here, we successfully synthesized a portfolio of aqueous GGS nanoparticles (NP) with excellent stability through a one-step, reproducible synthesis: Anionic, cationic, and protein-coated GGS NPs were obtained by using 3-mercaptopropionic acid (3MPA), branched poly(ethyleneimine) (bPEI) and bovine serum albumin (BSA) as a coating. All GGS NPs comprise small (<10 nm) and large anisotropic (>30 nm) morphologies and display two absorption bands centered at 530–540 nm and 800–900 nm. The photoacoustic activity (PA) of GGS NPs in solution at the visible (532 nm) and NIR (800 nm) region is similar and independent of the coating. Remarkably, they outperformed the spherical gold NPs and performed comparable to GNRs. *In vitro* PA microscopy images recorded with visible and NIR lasers revealed that GGS NPs are successfully internalized by triple-negative MDA-MB-231 breast cancer cells, used for the proof of principle. A coating-dependent intracellular PA signal in favor of GGS-3MPA was observed. The weakest signal was obtained with the GGS-BSA, indicating a low cellular uptake. These stable, aqueous GGS NPs emerge as promising candidates for broad-band PAI and further biomedical applications.

Received 27th August 2024,
Accepted 14th November 2024

DOI: 10.1039/d4nr03509g

rsc.li/nanoscale

Introduction

Photoacoustic imaging (PAI) is quite an exciting emerging technique in medicine, combining the advantages of optical and ultrasound imaging in a single modality, offering both high contrast and high resolution.[1] Tomographic, microscopic, and endoscopic approaches are proposed depending on the field of view, depth, and resolution demands, which highly vary depending on the sample of interest. The contrast in PAI originates from several cascaded physical events: it starts with the absorption of a nanosecond laser pulse, creating a rapid thermoelastic expansion that finally generates pressure waves. Pixel-wise scanning of the sample while recording the pressure waves with a conventional ultrasonic transducer forms the

[a]*Department of Chemistry, Koç University, Sarıyer, İstanbul, 34450, Türkiye. E-mail: fyagci@ku.edu.tr*
[b]*Department of Physics, Boğaziçi University, Bebek, İstanbul, 34342, Türkiye. E-mail: natali.sozudogru@boun.edu.tr*
[c]*Center for Life Sciences and Technologies (LifeSci), Boğaziçi University, İstanbul, 34342, Türkiye*
[d]*Faculty of Engineering, Özyeğin University, Çekmeköy, İstanbul, 34794, Türkiye. E-mail: burcin.unlu@ozyegin.edu.tr*

†Electronic supplementary information (ESI) available: Time-dependent absorbance spectra of the reaction mixture following the progress of GGS formation and growth in the absence of a coating material; thermogravimetric analysis of GGS-3MPA, GGS-bPEI, and GGS-BSA; TEM images of GGS-bPEI, its magnified section, and lattice spacing; TEM images of GGS-BSA, magnified section, and lattice spacing; size analysis of GGS-3MPA, GGS-bPEI, and GGS-BSA NPs from TEM images; XRD of GGS-3MPA, GGS-bPEI, and GGS-BSA; the absorbance of GGS-3MPA, GGS-bPEI, GGS-BSA, and their hydrodynamic size and zeta potential after the first day of synthesis and one year later in the dark and +4 °C conditions; absorbance of GGS-3MPA, GGS-bPEI, GGS-BSA, and their hydrodynamic size and zeta potential followed for four weeks in the dark and +37 °C conditions; pictures of GGS-3MPA, GGS-bPEI, and GGS-BSA solutions in PBS and DMEM; hydrodynamic size and zeta potential of GGS solutions in PBS; raw PA Signal of GGS-3MPA, GGS-bPEI, GGS-BSA at 532 nm laser exposure; raw PA Signal GGS-3MPA, GGS-bPEI, GGS-BSA at 800 nm laser exposure; dose-dependent cell viability of L929 and MDA-MB-231 cells treated with GGS-3MPA, GGS-bPEI, and GGS-BSA after 48 h incubation; absorbance of GNP; absorbance of GNR, TEM image of GNR; photoacoustic signal efficiencies of GGS, GNP, and GNR; experimentally measured edge and line spread functions at 800 and 532 nm wavelengths; absorbance spectrum of small and large GGS-3MPA NPs separated via centrifugation. See DOI: https://doi.org/10.1039/d4nr03509g

‡M.D. and M.N.C. contributed equally to this work.

photoacoustic image. The amplitude of the emitted pressure waves is a function of the absorption coefficient (cm^{-1}), laser fluence (J cm^{-2}), and physical properties of the contrast agents (the Grüneisen parameter). Unlike fluorescent imaging or MRI, which requires luminescent or magnetizable nanoparticles, photoacoustic microscopy (PAM) emerged as the best-suited, versatile imaging modality for visualizing nanoparticles since it provides contrast based on their optical absorption.[2–4]

Nanoparticles (NP) with absorption in the near-infrared (NIR) region are especially valuable for PAI since scattering is less and penetration depth is high in the NIR region, favoring the visualization of deeply seated features, which is limited in optical imaging.[5–7] Plasmonic nanoparticles (nanocages, nanostars, nanorods),[8] semiconducting polymer nanoparticles,[9] and carbon-based nanomaterials[10] are known examples of NPs for PAI. Among these, plasmonic NPs are the most popular since the position of the surface plasmon resonance (SPR) peak may be tailored by controlling the particle size and morphology.[11] Rod-shaped gold nanoparticles have SPR peaks shifted from the visible to the near-infrared range.[12] However, the large aspect ratio causes enhanced scattering and collapse into spheres under moderate laser fluences (10 mJ cm^{-2}).[13,14]

Gold–gold sulfide (GGS) nanoparticles are not well-known in the literature but offer the characteristic SPR band of colloidal spherical gold NPs around 530 nm and a second, broader band between 650–1100 nm region.[15] Although a few successful synthesis approaches exist in the literature, the products had low colloidal stability and reproducibility in most cases.[16,17] Two potential causes could be the absence of a stabilizing coating during particle growth and the choice of the sulfur source. Sodium sulfide (Na_2S) is the most studied S-source. Still, although some reports use it fresh, it is usually aged before use, an ill-defined process, and a source of irreproducibility. Sodium thiosulfate is one of the products of the aging process, and it can potentially reduce the gold ions.[18] Zhang *et al.* reported GGS synthesis using $HAuCl_4$ and $Na_2S_2O_4$ (sodium thiosulfate), which produced small spherical and larger non-spherical particles with tunable NIR absorption *via* $HAuCl_4/Na_2S_2O_4$ ratio.[17] However, GGS NPs without a stabilizing coating lacked stability and aggregated at extended reaction times.

Aggregation of NPs may be prevented, and colloidal stability may be achieved by an *in situ* coating of the GGS, providing surface passivation and steric and/or electrostatic repulsion. Poly(ethylene glycol) derivatives are usually preferred for steric stabilization and biocompatibility.[19] Small molecules with charged functional groups, such as carboxylic acid or amine, provide electrostatic stabilization.[20] Polyelectrolytes are commonly used for electro-steric stabilization.[21] With multiple functional groups on their surface, proteins also serve as coating materials, providing high stability and biocompatibility of the NPs.[22,23] Coating materials also significantly influence NP properties such as optical properties, cytotoxicity, and cellular uptake, which are critical for medical applications.[24–27]

In this work, we first undertook the challenge of synthesizing colloidally stable GGS NPs. Then, we explored their potential as an exogenous contrast agent for PAM within the visible and near-infrared regions. The first challenge was achieved *via in situ* passivation of growing NP surfaces with various coating materials, producing a GGS portfolio with different surface chemistries. Anionic, cationic, and protein-coated GGS NPs were synthesized by using 3-mercaptopropionic acid (3-MPA), branched poly(ethyleneimine) (bPEI), and bovine serum albumin (BSA), respectively. Except for BSA, other coatings were combined with PEG-SH to ensure long-term stability. The influence of such coatings on colloidal stability, optical properties, cytotoxicity, and cellular uptake were studied. Over a year, no significant changes were observed in the hydrodynamic size or optical properties of the GGS NPs, confirming excellent colloidal and optical stability.

PAI potential of these GGS NPs was first evaluated in solution at both 532 nm and 800 nm, then *in vitro*. PAM provided valuable insight into the comparative cellular uptake of GGS NPs by triple-negative MDA-MB-231 breast cancer cells, used as a representative model, and pointed out the great potential of GGS NPs as a versatile broad-band PAI contrast agent.

In summary, this study represents a pioneering achievement by demonstrating a simple synthesis of a portfolio of aqueous, colloidally stable GGS NPs with a variety of surface chemistries exploitable in different biomedical applications and, to the best of our knowledge, the first demonstration of GGS NPs as attractive broad-band PAI contrast agents.

Results and discussion

Synthesis and characterization of GGS NPs

In the synthesis of typical gold NPs, borohydrides, carboxylic acids, alcohols, and sulfates can be listed as common agents used to reduce Au^{3+} or Au^{1+} to Au^0.[20] In the synthesis of GGS NPs, sodium thiosulfate was used as a reducing agent and sulfur source at a $HAuCl_4/Na_2S_2O_3$ molar ratio of 1.4.[18] During the reaction, after mixing $HAuCl_4$ and $Na_2S_2O_3$, the color changed from yellow to dark purple within the first few minutes. The absorbance spectrum of the growing NPs followed the progress of the reaction. The absorption peak intensities reached a maximum value at the 10th minute (Fig. S1†). At this point, the coating materials were added to prevent further growth and stabilize the NPs against aggregation.

Anionic GGS-3MPA NPs

In the case of anionic GGS-3MPA NPs, a small amount of mPEG-SH was added along with 3MPA to improve the colloidal stability of the NPs. GGS-3MPA were synthesized with 3MPA/mPEG-SH/Au mol ratios of 9/1/1. The hydrodynamic size of the GGS-3MPA was measured at around 3/64 nm (number/intensity-based average) by DLS, and the zeta potential was −34.1 mV (Table 1). GGS-3MPA showed a typical gold nanoparticle SPR band at around 530 nm and a broad NIR absorption at 880 nm (Fig. 1a).

Table 1 Hydrodynamic size and zeta potential of GGS NPs in water

Sample	Dh-number[a] (nm) intensity	Dh-intensity[b] (nm)	Zeta potential (mV)
GGS-3MPA	3.3	64.4	−34.1
GGS-bPEI	4.4	101.5	+8.9
GGS-BSA	40.9	107.7	+25.1

[a] Hydrodynamic size measured by DLS and reported as the number average. [b] Hydrodynamic sized measured by DLS and reported as the intensity average.

XPS analysis of the three different GGS NPs was also performed to elucidate the oxidation states of the Au and S atoms (Fig. 1b and c). Au $4f_{7/2}$ peak of GGS-3MPA appeared at the binding energy of 84.24 eV corresponding to metallic gold (Au^0). No other Au peak, such as Au^+, was detected. Such results agree with the literature and are attributed to the dominance of Au^0 over others and minimal peak separation between different oxidation states of Au.[16,28,29] The S $2p_{3/2}$ peak was at 162.85 eV, confirming the Au–S bond's existence.

The organic content of these NPs was determined to be 30% of the TGA thermogram (Fig. S2†). The lack of the S–H stretching band at around 2590–2560 cm^{-1} in the FTIR spectra confirmed the binding of the thiol group of 3-MPA and mPEG-SH on the GGS surface (Fig. 1d). The peak at 2856 cm^{-1} belongs to sp^3 hybridized C–H bonds. The stretching bands at 1721 cm^{-1} and 1142 cm^{-1} were assigned to the C=O stretching of carboxylic acid groups and the C–O stretching of PEG, respectively.[30,31]

TEM images show that the particle solution consists of small spherical and large non-spherical particles ranging in size and shape (Fig. 2a). Non-spherical particles were mostly triangles, truncated triangles, pentagons, and cuboctahedrons.

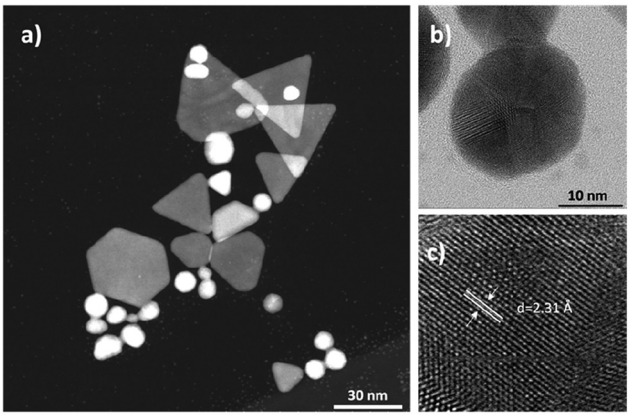

Fig. 2 TEM images of GGS-3MPA (a), magnified section (b), and lattice spacing (c).

D-Spacing of about 2.31 Å measured from the high-resolution TEM image of the GGS structures corresponds to (111)-type planes shown in Fig. 2c. Sizes measured from TEM images were consistent with the hydrodynamic sizes. Spherical particle diameters were around 2–3 nm, whereas the pseudo-spherical cuboctahedrons were around 20 nm. The edges of triangular and hexagonal plates were about 40 nm long (Fig. S4†). The diffraction pattern of GGS-3MPA corresponds to the (111), (200), (220), and (311) reflections of the face-centered-cubic (fcc) structure of gold (Fig. S5†).

Cationic GGS NPs

Cationic PEI is an attractive coating material for metal NP but has potential toxicity, which can be controlled by molecular weight and branching.[32] 10 kDa bPEI was used to synthesize cationic GGS NPs, which were sufficiently long to provide

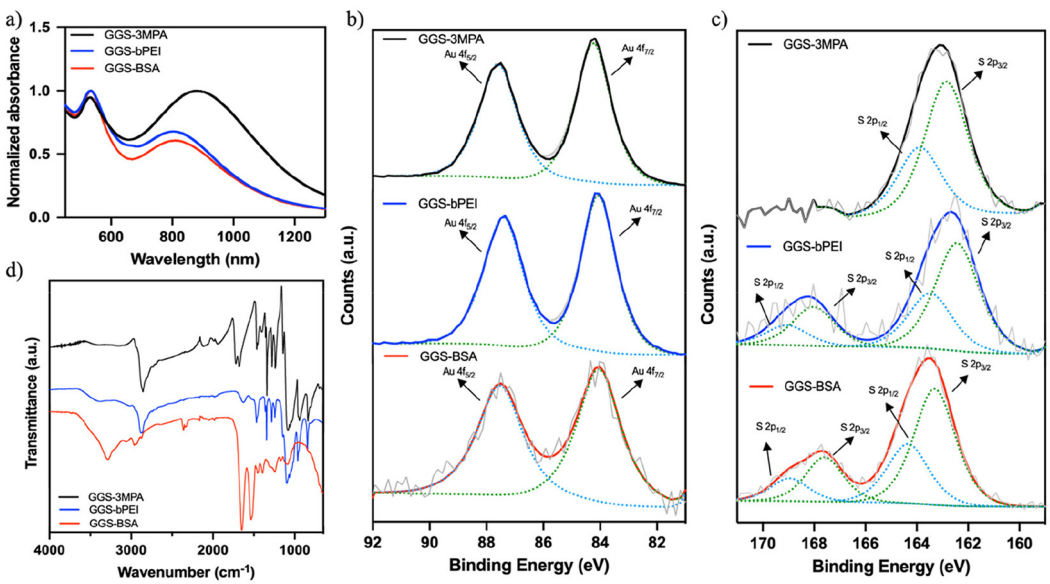

Fig. 1 (a) The UV–VIS spectra, (b) Au 4f and (c) S 2p XPS spectra, (d) FTIR spectra of the GGS-3MPA, GGS-bPEI, and GGS-BSA.

effective coating and stabilization and short enough to have cytocompatibility. It was also mixed with mPEG-SH to improve biocompatibility and aid stability. For GGS-bPEI, bPEI/mPEG-SH/Au mol ratios of 0.01/0.09/1 was used. GGS-bPEI had a hydrodynamic size of 4/102 nm (number/intensity-based average) and zeta potential of +8.9 mV (Table 1). The absorbance peaks of the particles were at 540 nm and 810 nm. NIR absorbance peak was narrower compared to GGS-3MPA.

XPS revealed a single Au $4f_{7/2}$ peak at the binding energy of 84.06 eV and two S $2p_{3/2}$ peaks at 162.43 eV and 168.02 eV, which can be assigned as metal-bound sulfur and sulfate arose from the oxidation on the outer surface (Fig. 1b and c).[33]

The organic content of GGS-bPEI was 35% (Fig. S2†). The FTIR spectrum showed a broad band of around 3400 cm^{-1} covering the N–H stretching of amine groups of bPEI. The sp^3 C–H stretching band was at 2877 cm^{-1} (Fig. 1d). The small shoulder peak at 1150 cm^{-1} showed the C–N bending of amines. Like GGS-3MPA, GGS-bPEI also consists of spherical and anisotropic particles (Fig. S3†), but the density of small spherical particles was higher than the larger non-spherical ones. *D*-Spacing of about 2.37 Å measured from the high-resolution TEM image of the GGS structures corresponds to (111)-type planes (Fig. S3†). The diameter of the spherical particles was around 3 nm, and the edges of anisotropic structures were 20 to 30 nm, with a few larger ones (Fig. S4†). The diffraction pattern of GGS-bPEI corresponds to the (111), (200), (220), and (311) reflections of the fcc gold (Fig. S5†).

Protein coated GGS-NPs

GGS-BSA nanoparticles were synthesized with BSA/Au mol ratios of 0.1/1. BSA was sufficient to stabilize the GGS alone due to its large molecular weight and large number and type of functional groups. Hence, the coating constitutes 70% of the NPs (Fig. S2†). GGS-BSA NPs had an overall cationic nature (+25.1 mV) and 41/108 nm (number/intensity-based average) hydrodynamic size (Table 1). These nanoparticles also showed two SPR bands at 540 nm and 820 nm.

XPS analysis showed that the Au $4f_{7/2}$ peak of GGS-BSA was at the binding energy of 84.04 eV, and the S $2p_{3/2}$ peak was at 163.3 eV and 167.6 eV (Fig. 1b and c). FTIR confirmed protein coating with 1648 cm^{-1} and 1534 cm^{-1} peaks characteristic of amide I and amide II vibrations of the BSA (Fig. 1d).[34,35] The band at 3290 cm^{-1} covers the peak of N–H stretching and broad -OH stretching of BSA.[36] Fig. S3† shows the TEM images of the GGS-BSA nanoparticles. The distribution of larger particles was higher compared to the other two coatings. *D*-Spacing of about 2.21 Å measured from the high-resolution TEM image of the GGS structures corresponds to (111)-type planes (Fig. S3†). The diameter of cuboctahedrons and edges of truncated triangles ranged from 20 to 70 nm (Fig. S4†). The diffraction pattern shows the (111), (200), and (220) reflections of the fcc gold (Fig. S5†).

Stability of GGS

In this study, we monitored the chemical and optical stability of synthesized GGS nanoparticles over a year. The nanoparticles were kept at 4 °C in the dark. Fig. S6† shows the absorbance, hydrodynamic size, and zeta potential of the GGS NPs. There was no appreciable change in the absorbance, peak positions, or hydrodynamic size of the GGS-3MPA, but the surface charge dropped to −6 mV. In the case of GGS-bPEI, the hydrodynamic size and the surface charge remained unchanged, but the NIR absorption slightly decreased with a 15 nm blue shift. GGS coated with BSA also sustained the hydrodynamic size, but both VIS and NIR absorption decreased, and the surface charge reduced from +25 mV to +15 mV. Their fundamental optical and structural properties remained unchanged despite minor changes within a year.

Further, GGS NPs were tracked for four weeks at physiological temperature in aqueous solutions (Fig. S7†). No significant changes in absorbance, hydrodynamic size, or surface charge were observed for GGS-3MPA or GGS-bPEI. However, storage of GGS-BSA at 37 °C for a long period of time is difficult, as expected. A minor decrease in absorbance was observed after one week, and hydrodynamic size increased in 3 weeks due to denaturation of the protein. The test was aborted at this point due to the gelation of BSA. GGS NPs were also kept in PBS and DMEM at 37 °C for 48 hours, and neither precipitation nor a significant color change was observed (Fig. S8a†). Additionally, no significant change was observed in the hydrodynamic size and zeta potential of GGS NPs in PBS (Fig. S8b†).

To demonstrate the stability of GGS nanoparticles under laser exposure, the PA signals were recorded at consecutive scans of the same sample. The signals scale nicely within the range of applied pulse energies, and no decrease in the raw PA signal was observed (Fig. S9†). This indicates excellent stability under laser exposure.

Cytotoxicity of GGS NPs

Cytotoxicity of the GGS NPs was tested between 20–500 μg GGS per mL concentrations on L929 healthy fibroblast and MDA-MB-231 breast cancer cells using the standard MTT assay after 24 h incubation (Fig. 3). GGS-3MPA and GGS-BSA were considered as safe to the cells in the studied concentration range. For GGS-BSA, a slight decrease in viability was observed above 300 μg GGS per mL. However, GGS-bPEI NPs significantly reduced cell viability above 100 μg GGS per mL for both

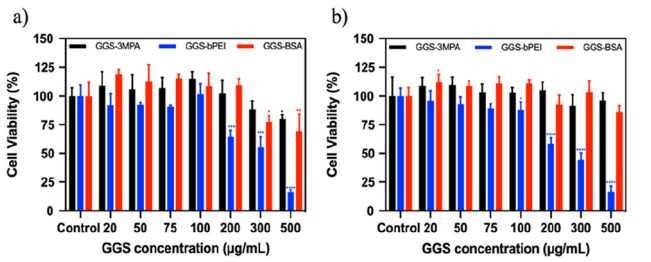

Fig. 3 Dose-dependent cell viability of (a) L929 and (b) MDA-MB-231 cells treated with GGS-3MPA, GGS-bPEI, and GGS-BSA after 24 h incubation. Control: untreated cells. Data were shown as mean ± SD (n = 5). Significance levels are indicated as follows: p = 0.0332 (*), p = 0.0021 (**), p = 0.002 (***), and p < 0.001 (****).

cell lines. The viability of L929 and MDA-MB-231 cells was also checked after 48 h incubation with GGS NPs using MTT assay (Fig. S10†). All studied GGS nanoparticles reduced the viability of L929 at and above 75 μg GGS per mL concentration. In the case of the MDA-MB-231 cells, only the cationic GGS-bPEI NPs showed dose-dependent cytotoxicity starting at 75 μg GGS-bPEI per mL after 49 h incubation.

Photoacoustic characterization of GGS NPs in solution

The photoacoustic wave generation potential of GGS nanoparticles was tested in their aqueous colloidal solutions at room temperature and compared with the performance of spherical gold nanoparticles (GNP) and gold nanorods (GNR). Glass tubes filled with NPs were laser scanned with the photoacoustic microscope shown in Fig. 4.

From the literature, the most simplified relation that relates the amplitude of the generated PA waves (p_0) to extinction coefficient (μ_e), laser fluence (J cm^{-2}) and Grüneisen parameter (Γ) is

$$p_0 \propto \Gamma F \mu_e \quad (1)$$

for molecular contrast agents. So, the amplitude of the emitted pressure waves in an individual imaging session scales with the extinction coefficient. However, the physical origin of the PA wave generation for nanometer-sized particles deviates from this simple thermoelastic expansion approach. It becomes sensitive to nanoparticle size, geometry, solvent, or coating. For example, the silica shell thickness on a GNP can significantly influence the generated PA waves. In one study, silica shell improved the PA signal 2.5 times at room temperature,[37] while in another study, decreasing PA amplitude with silica shell thickness was claimed.[38] These conflicting results led us to conduct a rigorous investigation of the generated PA wave intensities from the differently coated GGS NPs. In line with the absorption characteristics of these NPs, photoacoustic responses were measured at 532 nm and 800 nm with extinction coefficients of 0.25 mm^{-1} and 0.5 mm^{-1}. The amplitude of the generated PA signals with increasing incident pulse energy of the lasers was determined (Fig. 5). Spherical GNPs (15 nm, λ = 530 nm, Fig. S11†) and CTAB-coated GNRs (30/10 nm, λ = 770 nm, Fig. S12†) were also studied at 532 nm and 800 nm excitation, respectively, for comparison. The PA wave

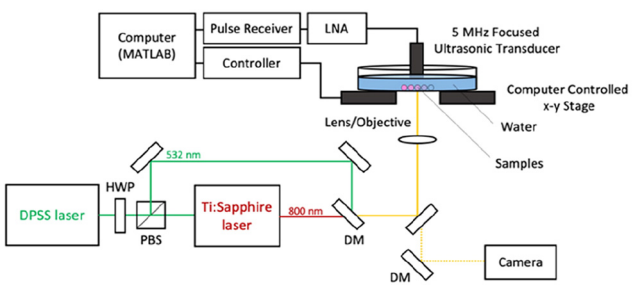

Fig. 4 Schematic illustration of the photoacoustic microscope (PAM) working at 532 and 800 nm. HWP: half-wave plate, PBS: polarizing beam splitter, DM: dichroic mirror, LNA: low-noise amplifier.

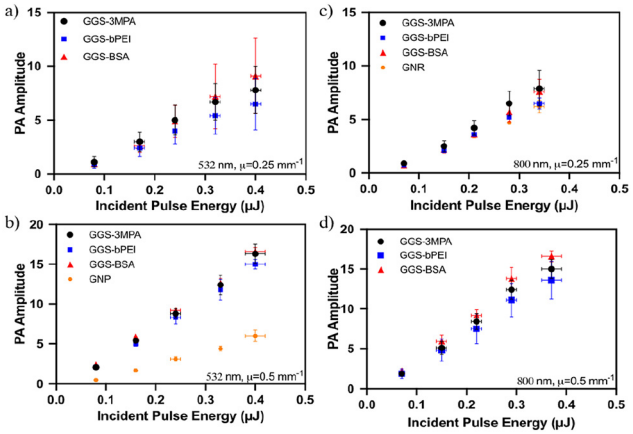

Fig. 5 Photoacoustic spectroscopy results of GGS samples having (a and c) 0.25 mm^{-1} and (b and d) 0.5 mm^{-1} extinction coefficients at 532 and 800 nm, respectively. Data were shown as mean ± SD (n = 3).

generation performance of the NPs was assessed *via* analysis of the slopes of the curves obtained for each NP (Table S1†). The results suggest negligible influence (<4%) of the GGS coating or the imaging wavelength on the generated PA amplitude. The performance of GGS NPs was comparable to that of GNRs at 800 nm. However, GGS NPs outperformed the GNPs by a factor of two at 532 nm. As a side note, we independently confirmed the literature that the GNRs are two times better PA emitters than GNPs.[39]

In vitro photoacoustic microscopy (PAM)

The potential application of the synthesized GGS NPs as a photoacoustic contrast agent was explored *in vitro* using the MDA-MB-231 breast cancer cell line as a model. Brightfield and PAM images acquired at 532 nm and 800 nm are presented in Fig. 6. Yellow shades in the PAM images represent the strength of the recorded PA signals on a logarithmic scale. The resolution of the PAM system at 532 nm was measured as

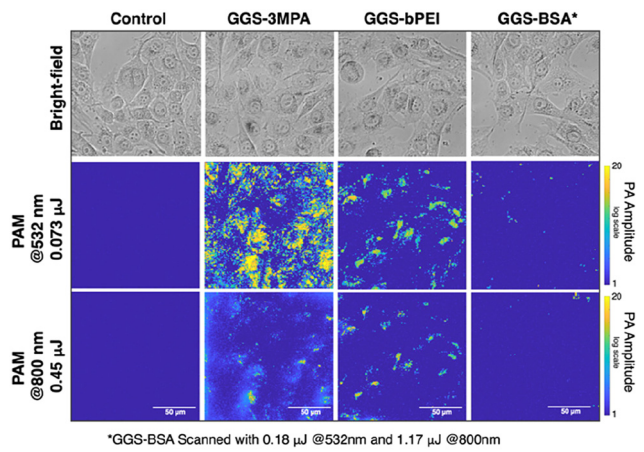

Fig. 6 PAM images of MDA-MB-231 cells treated with GGS NPs at λ = 532 and 800 nm. Blue corresponds to the background, and yellow shades represent the PA signal amplitude.

4 μm and 6 μm at 800 nm (Fig. S13†). Since all GGS NPs emit similar PA waves under the same laser pulse energy exposure (Fig. 5), a direct comparison of the measured contrast strength across the samples and scanned wavelengths can be done confidently. Breast cancer cells (MDA-MB-231) treated with the GGS NP at the safe dose (100 mg mL^{-1}) were scanned with 532 nm (0.073 μJ) and 800 nm (0.45 μJ) lasers. Based on the images obtained with 532 nm laser exposure, cancer cells differentiated the GGS NPs. A strong intra-cellular signal was observed in GGS-3MPA-treated cells, but no appreciable PA signal was observed in GGS-BSA-treated cells. GGS-PEI provided significant contrast but not as strong as GGS-3MPA. Despite having similar bulk PA activity, such a difference in intracellular signal suggests a differential cellular uptake of the NPs. Although BSA enhances biocompatibility and acts as a nutrient for cells, in our case, such a low uptake may be attributed to the large particle size of GGS-BSA particles.[40,41] Imaging in the NIR required almost six times higher laser pulse energy (0.45 μJ) to generate an intracellular PA contrast comparable to the one obtained at 532 nm.

GGS-3MPA with the strongest PAM contrast was centrifugated to separate the large and small particles. Although a complete separation was not possible, two populations, one with stronger and the other with weaker NIR absorbance in addition to the visible SPR band, were obtained (Fig. S14†). GNRs also exhibit two major SPR bands where short and long dimensions are responsible for visible and NIR absorption.[4]

TEM images of the MDA-MB-231 cells treated with GGS-3MPA showed both small spherical NPs (Fig. 7a) and large anisotropic NPs (triangular, hexagonal, cuboctahedral) (Fig. 7b) in the cells, supporting PA activity in a broad spectrum, *i.e.*, visible and NIR. Although a conclusion towards differential uptake favoring small spherical GGS is not possible, especially since there are more spherical particles observed in the TEM of the synthesized GGS, a lot of small particles, some of which aggregated in the cells, were noticed, which may be increasing the local concentration, hence the contrast at 532 nm (Fig. 7a).

Overall, GGS-3MPA and GGS-PEI NPs may be utilized as contrast agents for photoacoustic microscopy/imaging applications in the visible and NIR wavelengths and may provide information about NP internalization.

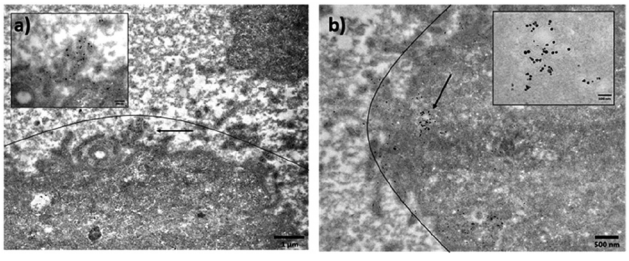

Fig. 7 TEM images of cross-sectioned MDA-MB-231 cells treated with GGS-3MPA. Lines drawn around the cell are a guide to differentiate the cells.

Conclusions

We first successfully produced colloidally stable, biocompatible, aqueous GGS NPs with strong visible and NIR absorbance in the present study. Then, we demonstrated their potential as exogenous contrast agents for photoacoustic imaging both in the visible and NIR wavelengths.

Stable GGS NPs were produced in a one-step, aqueous synthesis utilizing functional 3MPA, bPEI, BSA, and PEG-SH as coating materials. All compositions were colloidally and optically stable over a year. TEM images suggest that synthesized GGS nanoparticles comprise small spherical and large non-spherical geometries, which agree well with strong absorption at around 530 and 800 nm, suitable for PA imaging.

The PA activity of the GGS NPs measured in aqueous solutions at 532 and 800 nm indicated no significant impact of the coating or the scanning wavelength on the generated PA amplitude. However, they were two times better than well-known PA emitters spherical GNPs at 532 nm and slightly better than GNRs at 800 nm.

All GGS NPs were safe up to 100 μg GGS per mL for MDA-MB-231 cancer cells and healthy L949 cells, chosen as examples for the proof of principle in this study. Only cationic GGS-bPEI showed significant toxicity above 100 μg GGS per mL, which aligns with the literature on the potential higher toxicity of cationic nanoparticles.

Photoacoustic microscopy of the cells treated with GGS NPs at the non-toxic dose confirmed signal generation at both imaging wavelengths and provided insight into the relative cellular uptake of differently coated/sized GGS NPs in MDA-MB-231 cells. Unlike GGS-BSA NPs, GGS-3MPA and GGS-bPEI produced notable contrast at both wavelengths, but imaging at 800 nm required a stronger laser power. No contrast generation in the cells treated with GGS-BSA suggested no cellular uptake, possibly due to the larger sizes of this NP. Among all three GGS NPs, the strongest contrast was produced by GGS-3MPA NPs at both imaging wavelengths, but the signal amplitude was six times higher at 532 nm than at 800 nm. TEM images of GGS-3MPA-treated cells confirmed endocytosis of small spherical and large anisotropic nanoparticles.

These results suggested that cells internalize all different morphologies of the prepared GGS NPs, rendering them as broad-band PAI contrast agents. This is the first time we know that GGS nanoparticles are shown as PAI contrast agents in the near-infrared window.

Experimental section

Materials

Gold(III) chloride trihydrate ($HAuCl_4 \cdot 3H_2O$) and sodium thiosulfate ($Na_2S_2O_3$) were purchased from Sigma–Aldrich. 3-Mercaptopropionic acid (3-MPA) was provided by Merck. Bovine serum albumin (BSA) was bought from GenDEPOT (USA). Branched poly(ethyleneimine) (bPEI) with an average molecular weight of 10 kDa was obtained from Polysciences

(USA). Methoxy poly(ethylene glycol) thiol (mPEG-SH) (2 kDa) was from Laysan Bio, Inc. (USA). Ultracentrifuge tubes with polysulfone filtration membranes (10, 30, and 100 kDa) were from Sartorius (Germany). All chemicals were of the highest purity or analytical grade, and only ultra-pure water was used (18.2 MΩ, Rephile Bioscience, and Technology, Shanghai, China).

Dulbecco's Modified Eagle Medium (DMEM), fetal bovine serum, trypsin-EDTA, L-glutamine, and penicillin–streptomycin were purchased from Diagnovum (Germany). Dimethyl sulfoxide Hybri-Max™ was from Sigma (USA). Phosphate-buffered saline (PBS) tablets and thiazolyl blue tetrazolium bromide (MTT) were obtained from Bio-matik Corp. (Canada). Paraformaldehyde solution (4%) in PBS was bought from Santa Cruz Biotechnology, Inc. (USA). 96-Well plates were obtained from Nest Biotechnology Co. Ltd (China). MDA-MB-231 human breast cancer cells were provided by Gozuacik Lab (Koç University Hospital, Istanbul, Türkiye).

Synthesis of gold–gold sulfide nanoparticles

Stoichiometry and concentration of $HAuCl_4$ and $Na_2S_2O_3$ solutions were adopted from the literature.[17] 6.6×10^{-3} mmol $Na_2S_2O_3$ solution was rapidly added into 8.55×10^{-3} mmol $HAuCl_4$. After 10 min of reaction, aqueous coatings solutions were injected into the solution under vigorous stirring (500 rpm) at room temperature (RT). The cationic GGS (GGS-bPEI), bPEI, and mPEG-SH mixture at bPEI/mPEG/Au mol ratios of 0.01/0.09/1 was used. For the anionic GGS (GGS-3MPA), 3MPA and mPEG–SH mixture at 3MPA/mPEG/Au mol ratios of 9/1/1 was used. For the protein-coated GGS (GGS-BSA), only BSA was used at 0.1/1 : BSA/Au mol ratios. At the end of the 30-minute reaction, NP solutions were washed with DI water using centrifugal filters (for GGS-3MPA 10 kDa, GGS-bPEI 30 kDa, GGS-BSA 100 kDa cut-off) to remove excess chemicals and stored in the dark at 4 °C.

Separation of small and large GGS NPs

Synthesized GGS NPs were centrifuged at 1000 rpm for 5 minutes in 3 cycles. The supernatant and the pellet were separated for investigation.

Synthesis of GNP and GNR

GNP and GNR were used for comparison and synthesized by already published procedures. The synthesis of spherical, PEI-coated cationic, spherical gold nanoparticles (GNP) was adapted from Cavuslar *et al.*[42] GNR was synthesized by Dr Canbek according to a published procedure by Ozdil *et al.*[43]

Characterization

Thermal gravimetric analysis (TGA) was performed using TA Q500 to determine the organic content of GGS NPs. Dried samples were heated from room temperature to 900 °C with a ramping rate of 10 °C min^{-1} in a nitrogen atmosphere. An isothermal step at 100 °C was added to the procedure to remove the adsorbed humidity from the sample. Once the organic content of NPs is determined, it is subtracted from the overall nanoparticle amount to determine the inorganic content of the NPs. In the *in vitro* experiments, the inorganic content of GGS NPs was used for dose-dependent studies.

The absorption spectrum of the GGS variants was measured by a Shimadzu UV-VIS-NIR spectrophotometer between 450 and 1300 nm. Malvern Zetasizer Nano ZS measured hydrodynamic sizes and zeta potentials. Surface analysis of GGS NPs was performed with a Thermo K-Alpha X-Ray Photoelectron Spectrometer. Bruker D8 Advanced X-Ray Diffractometer analyzed the crystallographic structure of the NPs. Functional group determination was done by Thermo Scientific iS10 FT-IR instrument in the wavenumber range between 650–4000 cm^{-1} with a resolution of 4 cm^{-1}. Particle sizes and shapes were confirmed with Hitachi 7800 TEM analysis.

Photoacoustic evaluation in solutions

The photoacoustic wave generation potential of GGS was studied with a homemade optically resolved photoacoustic microscope (OR-PAM). The samples having two extinction coefficients (m = 0.5 mm^{-1} and 0.25 mm^{-1}) were filled into glass tubes (1.1 mm inner diameter). They were placed side by side in a water-filled Petri dish (Fig. 4). For the visible range, a 10 kHz, 532 nm laser (Spectra-Physics, Explorer One) having pulse energies between 0.1 to 0.5 mJ (4–20 mJ cm^{-2}) was loosely focused with a 50 mm lens on the samples. Each sample was scanned three times. A custom-made gain-switched Ti: Sapphire laser operating at 800 nm was used for the NIR range. Emitted acoustic waves were received through a 5 MHz single-element ultrasonic transducer and amplified (50 dB) with a two-stage amplification scheme in both experiments. Recorded PA signals with respect to the incident laser pulse energy were plotted, and the slope of respected curves was used for comparison.

Cell culture

L929 healthy fibroblast and MDA-MB-231 triple-negative breast cancer cells were cultured in DMEM medium supplemented with 10% fetal bovine serum, 2% L-glutamine (2 mM), and 1% penicillin–streptomycin at a 37 °C incubator with 5% CO_2 atmosphere. Cells were washed with PBS and trypsinized with 0.05% trypsin-EDTA before passage and seeding.

Cytotoxicity assay

MTT metabolic activity assay was used to determine the cytotoxicity of GGS NPs. NP solutions were sterilized by 0.2 μm sterile filters before treatment. L929 and MDA-MB-231 cells were seeded into 96-well plates with 1×10^4 cell per well density. After overnight incubation, the medium was replaced with a fresh medium, and NPs were added to cells at 20–500 μg ml^{-1} concentration (based on the inorganic content determined by TGA measurement). Cytotoxicity was measured after short and long incubation times. After 6 h and 24 h incubation, the medium of the cells was removed, and wells were washed with PBS. 50 μL MTT reagent (5 mg mL^{-1} in PBS) and 150 μL medium were added to wells and incubated for 4 h. After formazan crystals are formed by viable cells, they are dis-

solved by adding 200 μL of ethanol : DMSO (1 : 1 v/v) solution. The absorbance of the solution was measured by Synergy H1, Biotech Instruments microplate reader at 570 nm, which has a reference reading at 650 nm. The viability of the cells was calculated using the following equation:

$$\text{Cell viability}\,(\%) = \left[\frac{\text{Absorbance (treated)}}{\text{Absorbance (control)}}\right] \times 100 (n = 5) \quad (2)$$

TEM of the cells treated with GGS

MDA-MB-231 cells were seeded into 6-well plates with 2×10^5 cell per well density. After overnight incubation, cells were treated with 50 μg mL^{-1} GGS-3MPA for 24 h. After treatment, the medium of the cells was removed, and the cells were washed with PBS three times and trypsinized. The cell suspension was transferred to an Eppendorf tube and centrifuged (1500 rpm, 5 min). The solution was decanted, and the cell pellet was redispersed in a phosphate buffer. Then, the suspension was centrifuged, and the solution was decanted and redispersed into 2.5% glutaraldehyde solution for fixation for 1 h. The cell pellet was washed with phosphate buffer and fixed with post-fixative osmium tetroxide solution for 1 h. The fixed pellet was washed and stained with uranyl acetate for 1 h and washed with deionized water. The pellet was embedded into filtered egg white, centrifuged, and the excess egg white was removed. 70% alcohol solution was added to the sample and kept at 4 °C for 2 days. The pellet was washed with 90%, 100%, and 100% ethanol for 10 min each. The sample was treated with propylene-Epon (Canemco Inc., Quebec, Canada) solution for 1 h. Then, the sample was embedded in pure Epon for 1 h and thin-sectioned. These sections were collected on copper grids and visualized with Hitachi HT7800 120 kV (S) TEM.

In vitro photoacoustic microscopy (PAM)

MDA-MB-231 cells were seeded with 2×10^5 cell per well density into glass bottom plates and incubated overnight. The following day, the medium of the cells was removed, and GGS-3MPA, GGS-bPEI, and GGS-BSA were added to wells at a 100 μg mL^{-1} concentration with fresh medium and incubated for 24 h. The medium of the cells was removed, cells were washed with PBS three times, and 4% paraformaldehyde solution was added to fix the cells. After 20 min incubation of the cells at RT, the paraformaldehyde solution was removed, and cells were washed with PBS three times.

The PAM setup shown in Fig. 4 was slightly modified for cellular imaging. The focusing lens was replaced with a 40× objective, and a camera (Thorlabs (DCU224M-GL)) was added. A custom-made MATLAB code (SN: 1076960) simultaneously translated the motorized stages, and a DAQ card (Gage Compuscope) recorded the emitted signals. Later, the maximum amplitude projection method was applied to the pixel-wise recorded signals to form the photo-acoustic microscopy images.

Statistical analysis

Tukey's multiple comparison tests were used for the statistical analysis of MTT (GraphPad Software, Inc., USA). All data were expressed as mean ± standard deviation (SD), and $p < 0.05$ was considered statistically significant.

Author contributions

H.Y.A. and M.B.Ü. conceptualized the idea and edited the manuscript. M.D. and D.S. synthesized GGS and GNP nanoparticles and performed the characterization. M.D. performed *in vitro* toxicity and uptake studies. M.N.C. and A.K. performed the PAM measurements. M.D. and M.N.C. wrote the manuscript. All authors have approved the final version of the manuscript.

Data availability

The datasets generated during and/or analyzed during the current study are available from the corresponding author upon reasonable request.

Conflicts of interest

There are no conflicts to declare.

Acknowledgements

This work was supported by TUBITAK, the Scientific and Technological Council of Türkiye under grant 119F319, and the State Planning Organization of Türkiye (DPT) under grant 2009K120520. Alireza Khoshzaban acknowledges funding from the European Union's Horizon 2020 research and innovation program under grant agreement No 812780. The authors would like to acknowledge Asst. Prof. C. Canbek for providing the gold nanorods for comparison purposes, to KUYTAM for providing the Zetasizer, XPS, FTIR, and XRD equipment to characterize the synthesized nanoparticles, and to Dr G. Çorapçıoğlu and S. Demir for TEM analysis.

References

1 D. Das, A. Sharma, P. Rajendran and M. Pramanik, Another decade of photoacoustic imaging, *Phys. Med. Biol.*, 2021, **66**(5), 05TR01.
2 J. R. Cook, W. Frey and S. Emelianov, Quantitative Photoacoustic Imaging of Nanoparticles in Cells and Tissues, *ACS Nano*, 2013, **7**(2), 1272–1280.
3 I. Steinberg, D. M. Huland, O. Vermesh, H. E. Frostig, W. S. Tummers and S. S. Gambhir, Photoacoustic clinical imaging, *Photoacoustics*, 2019, **14**, 77–98.

4 S. N. Liao, W. Yue, S. N. Cai, Q. Tang, W. T. Lu, L. X. Huang, T. T. Qi and J. F. Liao, Improvement of Gold Nanorods in Photothermal Therapy: Recent Progress and Perspective, *Front. Pharmacol.*, 2021, **12**, 664123, DOI: 10.3389/fphar.2021.664123.
5 R. Weissleder, A clearer vision for in vivo imaging, *Nat. Biotechnol.*, 2001, **19**(4), 316–317.
6 Y. Lyu, J. C. Li and K. Pu, Second Near-Infrared Absorbing Agents for Photoacoustic Imaging and Photothermal Therapy, *Small Methods*, 2019, **3**, 1900553.
7 Y. S. Chen, Y. Zhao, S. J. Yoon, S. S. Gambhir and S. Emelianov, Miniature gold nanorods for photoacoustic molecular imaging in the second near-infrared optical window, *Nat. Nanotechnol.*, 2019, **14**(5), 465–472, DOI: 10.1038/s41565-019-0392-3.
8 Y. J. Liu, P. Bhattarai, Z. F. Dai and X. Y. Chen, Photothermal therapy and photoacoustic imaging via nanotheranostics in fighting cancer, *Chem. Soc. Rev.*, 2019, **48**(7), 2053–2108, DOI: 10.1039/c8cs00618k.
9 K. Y. Pu, A. J. Shuhendler, J. V. Jokerst, J. G. Mei, S. S. Gambhir, Z. N. Bao and J. H. Rao, Semiconducting polymer nanoparticles as photoacoustic molecular imaging probes in living mice, *Nat. Nanotechnol.*, 2014, **9**(3), 233–239, DOI: 10.1038/Nnano.2013.302.
10 K. Yang, L. L. Hu, X. X. Ma, S. Q. Ye, L. Cheng, X. Z. Shi, C. H. Li, Y. G. Li and Z. Liu, Multimodal Imaging Guided Photothermal Therapy using Functionalized Graphene Nanosheets Anchored with Magnetic Nanoparticles, *Adv. Mater.*, 2012, **24**(14), 1868–1872, DOI: 10.1002/adma.201104964.
11 K. L. Kelly, E. Coronado, L. L. Zhao and G. C. Schatz, The optical properties of metal nanoparticles: The influence of size, shape, and dielectric environment, *J. Phys. Chem. B*, 2003, **107**(3), 668–677.
12 X. H. Huang, S. Neretina and M. A. El-Sayed, Gold Nanorods: From Synthesis and Properties to Biological and Biomedical Applications, *Adv. Mater.*, 2009, **21**(48), 4880–4910, DOI: 10.1002/adma.200802789.
13 H. Moon, D. Kumar, H. Kim, C. Sim, J. H. Chang, J. M. Kim, H. Kim and D. K. Lim, Amplified Photoacoustic Performance and Enhanced Photothermal Stability of Reduced Graphene Oxide Coated Gold Nanorods for Sensitive Photo acoustic Imaging, *ACS Nano*, 2015, **9**(3), 2711–2719.
14 J. P. Sun, Y. T. Ren, K. Wei, M. J. He, B. H. Gao and H. Qi, Photoacoustic response optimization of gold nanorods in the near-infrared region, *Results Phys.*, 2022, **34**, 105209.
15 M. C. Tan, J. Y. Ying and G. M. Chow, Structure and microstructure of near infrared-absorbing Au–Au2S nanoparticles, *J. Mater. Res.*, 2007, **22**(9), 2531–2538.
16 T. Morris, H. Copeland and G. Szulczewski, Synthesis and characterization of gold sulfide nanoparticles, *Langmuir*, 2002, **18**(2), 535–539.
17 G. Zhang, J. B. Jasinski, J. L. Howell, D. Patel, D. P. Stephens and A. M. Gobin, Tunability and stability of gold nanoparticles obtained from chloroauric acid and sodium thiosulfate reaction, *Nanoscale Res. Lett.*, 2012, **7**(1), 1–9.
18 A. M. Schwartzberg, C. D. Grant, T. van Buuren and J. Z. Zhang, Reduction of HAuCl4 by Na2S revisited: the case for Au nanoparticle aggregates and against Au2S/Au core/shell particles, *J. Phys. Chem. C*, 2007, **111**(25), 8892–8901.
19 M. Ali Dheyab, A. Abdul Aziz, M. S. Jameel, P. Moradi Khaniabadi and A. A. Oglat, Rapid sonochemically-assisted synthesis of highly stable gold nanoparticles as computed tomography contrast agents, *Appl. Sci.*, 2020, **10**(20), 7020.
20 C. D. De Souza, B. R. Nogueira and M. E. C. Rostelato, Review of the methodologies used in the synthesis gold nanoparticles by chemical reduction, *J. Alloys Compd.*, 2019, **798**, 714–740.
21 O. Çavuşlar and H. Y. Acar, Other Polymers, in *Reducing Agents in Colloidal Nanoparticle Synthesis*, 2021, pp. 276–315.
22 M. N. Martin, A. J. Allen, R. I. MacCuspie and V. A. Hackley, Dissolution, agglomerate morphology, and stability limits of protein-coated silver nanoparticles, *Langmuir*, 2014, **30**(38), 11442–11452.
23 S. Rana, A. Bajaj, R. Mout and V. M. Rotello, Monolayer coated gold nanoparticles for delivery applications, *Adv. Drug Delivery Rev.*, 2012, **64**(2), 200–216.
24 M. Chanana and L. M. Liz-Marzan, Coating matters: the influence of coating materials on the optical properties of gold nanoparticles, *Nanophotonics*, 2012, **1**(3–4), 199–220.
25 S. Fraga, H. Faria, M. E. Soares, J. A. Duarte, L. Soares, E. Pereira, C. Costa-Pereira, J. P. Teixeira, M. de Lourdes Bastos and H. Carmo, Influence of the surface coating on the cytotoxicity, genotoxicity and uptake of gold nanoparticles in human HepG2 cells, *J. Appl. Toxicol.*, 2013, **33**(10), 1111–1119.
26 C. Freese, M. I. Gibson, H.-A. Klok, R. E. Unger and C. J. Kirkpatrick, Size-and coating-dependent uptake of polymer-coated gold nanoparticles in primary human dermal microvascular endothelial cells, *Biomacromolecules*, 2012, **13**(5), 1533–1543.
27 H. M. Fahmy, A. M. Mosleh, A. Abd Elghany, E. Shams-Eldin, E. S. A. Serea, S. A. Ali and A. E. Shalan, Coated silver nanoparticles: Synthesis, cytotoxicity, and optical properties, *RSC Adv.*, 2019, **9**(35), 20118–20136.
28 C.-L. Kuo and M. H. Huang, Hydrothermal synthesis of free-floating Au2S nanoparticle superstructures, *J. Phys. Chem. C*, 2008, **112**(31), 11661–11666.
29 F. Bensebaa, Y. Zhou, Y. Deslandes, E. Kruus and T. H. Ellis, XPS study of metal-sulfur bonds in metal-alkanethiolate materials, *Surf. Sci.*, 1998, **405**(1), L472–L476.
30 S. G. Lanas, M. Valiente, M. Tolazzi and A. Melchior, Thermodynamics of Hg2+ and Ag+ adsorption by 3-mercaptopropionic acid-functionalized superparamagnetic iron oxide nanoparticles, *J. Therm. Anal. Calorim.*, 2019, **136**(3), 1153–1162.
31 B. W. Chieng, N. A. Ibrahim, W. M. Z. Wan Yunus and M. Z. Hussein, Poly (lactic acid)/poly (ethylene glycol)

polymer nanocomposites: Effects of graphene nanoplatelets, *Polymers*, 2013, **6**(1), 93–104.

32 U. Lungwitz, M. Breunig, T. Blunk and A. Göpferich, Polyethylenimine-based non-viral gene delivery systems, *Eur. J. Pharm. Biopharm.*, 2005, **60**(2), 247–266.

33 G. Beamson, High resolution XPS of organic polymers. *The Scienta ESCA 300 Database* 1992.

34 M. J. Baker, J. Trevisan, P. Bassan, R. Bhargava, H. J. Butler, K. M. Dorling, P. R. Fielden, S. W. Fogarty, N. J. Fullwood and K. A. Heys, Using Fourier transform IR spectroscopy to analyze biological materials, *Nat. Protoc.*, 2014, **9**(8), 1771–1791.

35 H. A. Alhazmi, FT-IR, spectroscopy for the identification of binding sites and measurements of the binding interactions of important metal ions with bovine serum albumin, *Sci. Pharm.*, 2019, **87**(1), 5.

36 Y. Ji, X. Yang, Z. Ji, L. Zhu, N. Ma, D. Chen, X. Jia, J. Tang and Y. Cao, DFT-calculated IR spectrum amide I, II, and III band contributions of N-methylacetamide fine components, *ACS Omega*, 2020, **5**(15), 8572–8578.

37 Y. S. Chen, W. Frey, S. Aglyamov and S. Emelianov, Environment-Dependent Generation of Photoacoustic Waves from Plasmonic Nanoparticles, *Small*, 2012, **8**(1), 47–52, DOI: **10.1002/smll.201101140**.

38 G. A. Pang, F. Poisson, J. Laufer, C. Haisch and E. Bossy, Theoretical and Experimental Study of Photoacoustic Excitation of Silica-Coated Gold Nanospheres in Water, *J. Phys. Chem. C*, 2020, **124**(1), 1088–1098, DOI: **10.1021/acs.jpcc.9b09040**.

39 Y. J. Shi, S. H. Yang and D. Xing, Quantifying the Plasmonic Nanoparticle Size Effect on Photoacoustic Conversion Efficiency, *J. Phys. Chem. C*, 2017, **121**(10), 5805–5811, DOI: **10.1021/acs.jpcc.6b12498**.

40 K. Nambara, K. Niikura, H. Mitomo, T. Ninomiya, C. Takeuchi, J. J. Wei, Y. Matsuo and K. Ijiro, Reverse Size Dependences of the Cellular Uptake of Triangular and Spherical Gold Nanoparticles, *Langmuir*, 2016, **32**(47), 12559–12567, DOI: **10.1021/acs.langmuir.6b02064**.

41 R. Xing, S. Liu and S. Tian, Microwave-assisted hydrothermal synthesis of biocompatible silver sulfide nanoworms, *J. Nanopart. Res.*, 2011, **13**(10), 4847–4854.

42 O. Cavuslar, C. Celaloglu, F. D. Duman, Y. U. Konca, M. B. Yagci and H. Yagci Acar, pH and, molecular weight dependence of auric acid reduction by polyethylenimine and the gene transfection efficiency of cationic gold nanoparticles thereof, *New J. Chem.*, 2018, **42**(12), 10078–10083, DOI: **10.1039/c8nj00628h**.

43 Z. C. C. Ozdil, O. Spalla, N. Menguy and F. Testard, Competitive Seeded Growth: An Original Tool to Investigate Anisotropic Gold Nanoparticle Growth Mechanism, *J. Phys. Chem. C*, 2019, **123**(41), 25320–25330, DOI: **10.1021/acs.jpcc.9b05690**.